

Anomalous specific heat and magnetic properties of $\text{Tm}_x\text{Dy}_{1-x}\text{Al}_2$ ($0 \leq x \leq 1$)

Arjun K. Pathak,^{1,a} C. M. Bonilla,¹ D. Paudyal,¹ Y. Mudryk,¹ and V. K. Pecharsky^{1,2}

¹*The Ames Laboratory, U.S. Department of Energy, Iowa State University, Ames, Iowa
50011-3020, USA*

²*Department of Materials Science and Engineering, Iowa State University, Ames, Iowa
50011-2300, USA*

Abstract:

We study crystal structure, phase transitions and magnetism of pseudo-binary $\text{Tm}_x\text{Dy}_{1-x}\text{Al}_2$ ($0 \leq x \leq 1$) compounds using temperature dependent X-ray powder diffraction, specific heat and magnetization measurements, first principles, and model calculations. In low external magnetic fields, Dy-rich compounds undergo continuous, second-order phase transitions at the respective Curie temperatures, T_C . In contrast, the Tm-rich compounds exhibit discontinuous, first-order anomalies in the magnetically ordered states. These sharp transitions correlate with a substantial energy difference between the room temperature cubic and ground state rhombohedral structures of TmAl_2 . A clear anomaly in the lattice parameter is observed at ~ 30 K for $x = 0.5$, which nearly coincides with $T_C = 31.2$ K. The effective quadrupolar moment of the lanthanides changes sign around $x = 0.5$, which leads to a nearly zero anisotropy constant and approximately spherical effective $4f$ charge densities, providing an explanation for the lack of structural distortions below T_C for $x = 0.5$. The calculations confirm [001] as the easy magnetization axis in the ground state tetragonal structure of DyAl_2 , and reveal collapse of the orbital magnetic

^a apathak@ameslab.gov

moment when the easy magnetization direction changes to [111]. Within the rhombohedral ground state of TmAl_2 [111] is the easy magnetization direction.

Introduction

Rare earth (R) intermetallics show a wealth of interesting fundamental physics due to localized $4f$ electrons and spin-orbit coupling, which explains why these compounds remain an intriguing subject for materials science and condensed matter physics communities [1,2,3]. Within the broad intermetallic family, all rare earth dialuminides (RAl_2) adopt the same cubic Laves phase-type structure at room temperature but their ground states are represented by a number of differently distorted variants. With 78 possible $(R_xR'_{1-x})Al_2$ combinations, where R and R' represent different lanthanides, this group forms a rather unique playground to study and understand the interplay between magnetism and structure of $4f$ systems. Simple yet peculiar parent cubic Laves phase-type crystal structure, varying exchange and crystal field interactions, and anisotropic $4f$ charge densities of the lanthanides (except Gd^{3+} and Eu^{2+}), lead to an intricate competition between the closely related magnetism and crystallography. This often results in multiple metamagnetic transitions, glassy behaviors and short-range correlations [4,5,6,7,8, 9].

In mixed rare earth dialuminides one of the most studied effects is the consecutive appearance and disappearance of phase transitions as one lanthanide is partially replaced by another. The so-called DADA (disappearance, appearance, disappearance, appearance) behavior was initially observed in $Er_{1-x}Dy_xAl_2$ alloys [6]. The heat capacity (C_p) measurements of the latter showed emergence of an unexpected first order phase transition below Curie temperature (T_C) which is most pronounced around $x = 0.25$ and gradually disappears away from this specific concentration [6]. The observed behavior of C_p is consistent with the magnetic ac susceptibility measurements [7]. The discontinuity in the heat capacity, observed at certain concentrations of the alloying element Dy below T_C , was attributed to the competition between the magnetoelastic coupling

and quadrupolar effects; in contrast to the initial assumption that ascribed the second transition to a spin reorientation which occurs in the parent DyAl_2 [10]. Similar phenomenon is also observed in other pseudo-binary lanthanide systems, e.g. when Tb is partially replaced by Er, Tm, or Ho, when Er is replaced by Ho or Pr, and in a few other systems. This research brought along unexpected findings such as zero net magnetic moment in ferromagnetic $\text{Sm}_{1-x}\text{Gd}_x\text{Al}_2$ [11], exchange bias in $\text{Nd}_{0.75}\text{Ho}_{0.25}\text{Al}_2$ [12], glassy state below T_C and, recently, the discovery of the Griffiths-like phase and exchange bias in a mixed lanthanide $\text{Pr}_{0.6}\text{Er}_{0.4}\text{Al}_2$ [13].

A strong field dependence of the ac magnetic susceptibility under applied dc bias field in TmAl_2 has been reported [14] but the science of Tm-containing Laves phase compounds remains sparsely investigated and poorly understood. First principle calculations suggest that a first-order anomaly is expected when Dy is substituted by Tm in a pseudo-binary $\text{Tm}_x\text{Dy}_{1-x}\text{Al}_2$ when $x = 0.5$ [15]. In this work we study thermodynamic and magnetic properties of $\text{Tm}_x\text{Dy}_{1-x}\text{Al}_2$ alloys that show anomalous behavior below T_C . The analysis of experimental data coupled with theoretical results provides a general understanding of the nature of such anomalies.

Additionally, this study focuses on the intriguing phenomenon of magnetic frustration near T_C in Tm-rich compounds.

Experimental Details

Polycrystalline $\text{Tm}_x\text{Dy}_{1-x}\text{Al}_2$ ($0 \leq x \leq 1$) samples were prepared by arc melting of stoichiometric amounts of Tm, Dy, and Al metals in an inert argon atmosphere. Tm and Dy were obtained from the Materials Preparation Center, Ames Laboratory; both metals were at least 99.8 at.% pure with respect to all other elements in the periodic table. Commercially available Al was better

than 99.99 wt.% pure. To compensate for Tm (boiling temperature, $T_b \cong 2220$ K) and Dy ($T_b \cong 2840$ K) losses during the melting, 10 to 15 wt.% of Tm and 2 to 3 wt.% of Dy, depending upon alloy composition, were added during the arc melting. No additional heat treatment or annealing was needed to obtain single phase samples since these alloys melt congruently.

Room-temperature powder X-ray diffraction (XRD) measurements were performed on a PANalytical X'Pert Pro diffractometer utilizing Cu $K\alpha_1$ radiation. Powder XRD shows single phase samples with no detectable impurities. Microstructure and energy-dispersive x-ray spectroscopy (EDS) were carried out on a JEOL5910LV scanning electron microscope to verify the compositions of the samples. EDS and microscopy showed final sample compositions close to targeted concentrations of the main (Laves) phase along with minor inclusions of Tm-rich phases. The nearly linear dependence of lattice parameter on composition (Fig. 1b) also suggests the final sample compositions are close to the targeted stoichiometries. A Rigaku TTRAX rotating anode powder diffractometer utilizing Mo $K\alpha$ radiation was employed to measure temperature-dependent powder XRD patterns between 5 and 300 K in zero magnetic field for $Tm_{0.5}Dy_{0.5}Al_2$; the sample for these XRD experiments was prepared as described in Refs. 16. Rietveld refinements of all XRD data were performed using Rietica LHPM [17].

Heat capacity as a function of temperature, $C_p(T)$, was measured using both a homemade adiabatic heat-pulse calorimeter [18] and a Physical Property Measurement System (PPMS) from Quantum Design Inc. The measurements were carried out between 1.8 and 300 K at applied magnetic fields up to 100 kOe. Magnetic characterization, both DC and AC, was performed in a superconducting quantum interference device (SQUID) magnetic property

measurement system MPMS XL-7, Quantum Design Inc. For each sample the $M(T)$ data were recorded following three different protocols: 1) cooling the sample in zero field down to 1.8 K, then applying field and measuring the magnetization while warming up to room temperature (the zero-field cooled protocol, ZFC); 2) measuring the magnetization during cooling in the same applied field (the field-cooled cooling protocol; FCC); and 3) after cooling the sample down to 1.8 K in an external applied field, followed by measuring the magnetization during heating up to room temperature in the same field (field-cooled warming protocol, FCW). AC magnetic susceptibility as a function of temperature was measured with ac field 5 Oe amplitude at frequency 1 Hz in zero DC field. Magnetization values are accurate to within $\sim 1\%$ of the corresponding values [19].

Theoretical Calculations

The local spin density approximation including onsite $4f$ electron correlations [20] and spin orbit coupling (LSDA+ U +SOC) approach has been employed to calculate electronic structure and explain physical behaviors of $Tm_xDy_{1-x}Al_2$ compounds. This approach is implemented in the tight binding linear muffin tin orbital (TB-LMTO) [21] and full potential linear augmented plane wave (FP-LAPW) [22] band structure methods. Specifically, magnetocrystalline anisotropy calculations were performed employing LSDA+ U +SOC within FP-LAPW. The orbital dependent Coulomb and exchange interactions in LSDA+ U remove the degeneracy, and the $4f$ states split as prescribed by the tetrahedral site symmetry of R atoms, octahedral local symmetry of Al atoms, and the number of partially filled orbitals in both spin channels. Here, the spin orbit coupling of the $4f$ states of the heavy lanthanide atoms obeys $J = L+S$. The electronic structure

calculations performed with values of Hubbard U (on-site electron correlation parameter) ranging from 3.7 to 6.7 eV show that as expected, occupied $4f$ states shift to lower energy while unoccupied $4f$ states move to higher energy with increasing values of U . Unless stated otherwise, we used $U = 6.7$ eV and J (on-site $4f$ exchange) = 0.7, which are experimentally known values for gadolinium [19]. The k-space integrations with $16 \times 16 \times 16$ Brillouin zone mesh were sufficient for the convergence of total energies, magnetic moments, and $4f$ and $5d$ crystal field splitting. The electronic structure calculations of $\text{Tm}_x\text{Dy}_{1-x}\text{Al}_2$ were performed by converting the underlying symmetry of the crystal to the triclinic (P1) symmetry, and then different lanthanide atoms were placed depending upon the concentration into the eight R sites that are no longer formally connected by symmetry [15]. For example, for $\text{Tm}_{0.5}\text{Dy}_{0.5}\text{Al}_2$, 4 Tm and 4 Dy atoms were randomly placed in eight R formally independent positions inside a triclinic unit cell with $a = b = c$ and $\alpha = \beta = \gamma = 90^\circ$ that has the same unit cell volume as the cubic unit cell (for details, see Ref.15)

Experimental Results

Structural characterization

Room temperature XRD patterns were analyzed using Rietveld refinement and showed that a continuous solid solution $\text{Tm}_x\text{Dy}_{1-x}\text{Al}_2$ crystallizes in the MgCu_2 type cubic Laves phase structure at room temperature. No secondary phases were detected within the resolution of the technique (a pattern for $x = 0.95$ is shown as an example in Fig. 1a). Due to larger atomic radius of Dy compared to Tm, the lattice parameter increases linearly (Fig. 1b and Table 1) with Dy concentration from 7.773 for TmAl_2 to 7.843 Å for DyAl_2 ; the unit cell dimensions of both end members are commensurate with earlier reported values [23].

In order to check for a potential structural distortion, low temperature XRD patterns were collected for $\text{Tm}_{0.5}\text{Dy}_{0.5}\text{Al}_2$ while cooling the sample from 300 to 5 K, and full-profile Rietveld refinements were performed for each temperature. For example, the refined XRD pattern at $T = 9$ K is shown in Fig. 2a. The refinement results demonstrate that $\text{Tm}_{0.5}\text{Dy}_{0.5}\text{Al}_2$ retains the MgCu_2 -type Laves phase structure down to 5 K (Fig. 2a, b). The change in the cubic lattice parameter as a function of temperature is shown in Fig 2b. The lattice thermal expansion is nearly linear between 100 K and room temperature. A small but clear anomaly in the lattice parameter is observed at 30 K, which is close to the Curie temperature T_C (31.2 K). The absence of structural transformation in the sample with $x = 0.5$ is in agreement with the magnetization measurements and theoretical calculations presented later.

Heat capacity measurements

Heat capacity (C_p) was measured as a function of temperature in zero applied magnetic field for $\text{Tm}_x\text{Dy}_{1-x}\text{Al}_2$ with $0.25 \leq x \leq 1$ (heat capacity of DyAl_2 is reported in Ref. 24). When $0.25 \leq x \leq 0.85$ the $C_p(T)$ curves show broad maxima at low T , followed by rather sharp drops at the respective Curie temperatures, T_C (Fig. 3a-3d). The T_C shifts toward lower temperature as the Tm concentration increases. Additional $C_p(T)$ anomalies are observed in all measured compounds below T_C but are most pronounced when $x = 0.9$ and 0.95 (Figs. 3e-3f). The compound with $x = 0.25$ shows a rather broad anomaly centered at $T_1 \approx 24$ K (Fig. 3a) and a similar broad shoulder is also present for the $x = 0.5$ at a slightly lower temperature $T_1 \approx 20$ K (Fig. 3b). For $x = 0.75$ and 0.85 there are changes in $C_p(T)$ curvature, hinting at similar anomalies at the corresponding T_1 (Fig. 3c-3d), even though these are less visible because T_1 and

T_C become progressively closer. Lima *et al* [10] have reported a similar broad anomaly in the heat capacity of DyAl_2 single crystal. In the binary DyAl_2 , this broad, second-order anomaly has been attributed mainly to the spin reorientation from [100] to [111] direction [10]. The other end member of the series, TmAl_2 , also has a spin reorientation from [110] to [111] direction below T_C [25]. Figures 3e and 3f show much sharper peaks and with enhanced intensity below T_C for higher concentration of Tm ($x = 0.9$ and 0.95), the latter exhibiting two rather narrow peaks.

Thus, it is natural to consider the onset of these anomalies in the pseudo-binary compounds as a result of competition between two different spin reorientation processes that exist in the binary dialuminides. At the same time, it has been theoretically shown that the nature of anomalies in binary dialuminides is fundamentally different from pseudo-binary systems where a lanthanide with an oblate spheroid-shaped $4f$ charge density is mixed with another lanthanide with a prolate spheroid-shaped $4f$ charge density [15].

To get a better insight into the origin of the observed anomalies, $C_p(T)$ has been measured as a function of the temperature under external magnetic fields up to 30 kOe for $x \geq 0.85$. Figure 4 shows that the anomalous enhancements of C_p below T_C are gradually suppressed by the magnetic field. For $x = 0.85$ the kink at T_1 is no longer discernible in a field as low as 2.5 kOe, but for $x = 0.95$ a sharp low-temperature $C_p(T)$ peak is still present at 10 kOe. For all three high Tm concentrations ($x = 0.85, 0.9, \text{ and } 0.95$) T_C , taken as the main peak temperature, initially decreases with the increasing applied field, behaving as is typical for antiferromagnets (AFM). For example, for $x = 0.85$, T_C changes from 9.8 K in 0 to 7.7 K in 5 kOe magnetic field.

Heat capacity has been also measured as a function of temperature at different applied magnetic fields for the TmAl_2 parent (Fig. 5). The double peak structure is always present in the $C_p(T)$ data even with magnetic fields as high as 100 kOe (shown by arrows in C_p/T vs T curve in the inset of Fig. 5g). The higher temperature peak corresponds to the onset of long range magnetism. The peak at T_1 is ascribed to the spin reorientation transition. While the peak of $C_p(T)$ at T_C becomes broader in high applied fields, the peak at T_1 becomes visibly sharper in the middle range of applied fields (from 5 to 10 kOe). Curie temperature of TmAl_2 slightly decreases at first as the applied magnetic field increases, but when H exceeds 5 kOe, T_C begins to increase with field indicating that the system becomes a ferromagnet. In contrast to the unexpected and unusual field dependence of T_C , T_1 increases slowly with the field as commonly observed in conventional ferromagnets (Fig. 5h).

Magnetization

Magnetization as a function of field at 2 K for $x = 0, 0.25, 0.5, 0.75$ and 1 is shown in Fig. 6. All materials exhibit typical FM behavior with a negligible coercive field, similar to binary parents DyAl_2 [26] and TmAl_2 [27]. The values of saturated magnetization M_{sat} (Table I) have been obtained from extrapolation of M vs $1/H$ curves to $1/H = 0$. The obtained M_{sat} are lower than the calculated values for the mixtures of two trivalent ions $M_{\text{sat}} = x(gJ)_{\text{Tm}} + (1-x)(gJ)_{\text{Dy}}$ by 1 to 5%. These minor differences can be ascribed to weak anisotropy effects as well as to the interactions of rare-earth ions with local lattice environment or crystalline electric field (CEF). The influence of CEF on the measured magnetic moments is well known and has been also observed in other cubic rare earth based compounds such as $\text{RFe}_2\text{Zn}_{20}$, $\text{RCO}_2\text{Zn}_{20}$ ($R = \text{Y, Nd, Sm, Gd-Lu}$) [28],

RB_6 ($R = Ce, Pr, Nd$) [29], and $Er_{1-x}Dy_xAl_2$ [6]. For example, in $Er_{0.75}Tb_{0.25}Al_2$ the difference between experimental and calculated values of saturated magnetization reaches 12% [7].

Figure 7 shows the dc magnetization as a function of temperature $M(T)$ measured in 100 Oe applied magnetic field. All of the samples show step-like changes in the values of magnetization at T_C , which is expected for a magnetic order-disorder transition. T_C changes monotonically with the concentration scaling with the de Gennes factor (not shown). Values of T_C for each concentration coincide with the values obtained from $C_p(T)$ measurements (Table I).

Consistent with heat capacity data, behaviors of the $M(T)$ curves below T_C for $x \leq 0.75$ are different from those when $0.85 \leq x \leq 1$. This difference in the magnetic behaviors in these two ranges of concentration $0.85 \leq x \leq 1$ and $0 \leq x \leq 0.75$ is in agreement with different heat capacity behaviors. It is natural to conclude that two different processes dominate the magnetism in each range of concentration. All systems are FM or FM-like below T_C , however the effect of domain wall pinning is much stronger in the alloys with $0.25 \leq x \leq 0.75$ as reflected by the lambda shape of ZFC $M(T)$ curves below T_C . On the other hand, the ZFC $M(T)$ curves measured in compounds rich in Tm ($0.85 \leq x \leq 0.95$) show two abrupt changes in the ordered region: one at T_1 and a sharp decrease at T_C .

Magnetic irreversibility below T_C is evident in all samples when comparing the $M(T)$ data measured in ZFC, FCC, and FCW protocols. The anomalous transition at T_1 is more clearly identified in the $M(T)$ measured on the Tm rich samples, although in $TmAl_2$ the transition at T_1 becomes weak again. Thermal hysteresis between the FCC and FCW $M(T)$ curves decreases

with increasing the Tm concentration. Reduction of thermal hysteresis is also observed in higher dc applied magnetic fields, which remove domain wall pinning effect and suppress magnetic frustrations (discussed below). The sample with $x = 0.85$ shows a remarkable difference between the FCC and FCW magnetization in 100 Oe dc field (Fig. 7e). Figure 8 shows that thermal hysteresis for the sample with $x = 0.85$ diminishes when the dc applied field increases from 0.1 to 1 kOe. Presence of thermal hysteresis is often associated with first-order character of the transitions; however, the heat-capacity data shown in Fig. 3d rule this possibility out. Further, the FCW magnetization values are lower than those measured in the FCC regime, demonstrating that the magnetization is time-dependent. This result, together with the AFM-like behavior observed in field-dependent $C_p(T)$ curves shown in Fig. 4, indicates a possibility of magnetic frustration in pseudo-binary $Tm_xDy_{1-x}Al_2$ alloys similar to other RAI_2 systems [7].

AC magnetic-susceptibility measurements are commonly used to shed light on the dynamics of magnetic moments in the ordered state. Figure 9 shows the real component, χ'_{ac} , measured as a function of temperature in zero dc applied fields for all samples except the binary parents. The phase transitions at T_C are identified as the main peaks in the $\chi'_{ac}(T)$ curves. Above T_C a standard Curie-Weiss behavior is obeyed. The effective magnetic moment μ_{eff} , as well as Weiss temperatures, Θ_P , have been calculated for each system from the Curie-Weiss law by linear fits of the data to the equation $1/\chi'_{ac}(T) = (T - \Theta_P)/C$, where C is Curie-constant. Values of μ_{eff} and Θ_P derived from the Curie-Weiss fits are listed in Table I. The Weiss temperatures, Θ_P , coincide with T_C s determined from $M(T)$ and $C_p(T)$ curves. The effective magnetic moments are close to the values predicted by Hund's rule for the corresponding mixtures of non-interacting trivalent ions and the discrepancies caused by CEF effects are more pronounced for the Tm-rich samples,

in agreement with the magnetization measurements. AC magnetic susceptibility measurements also point to different magnetic responses for the Dy-rich ($x \leq 0.75$) and the Tm-rich compounds ($x \geq 0.85$) and the temperatures at which the anomalies are found in $M(T)$ and the $C_p(T)$ curves coincide with those from $\chi'_{ac}(T)$ curves.

Theoretical Investigation

The relative total energies of $TmAl_2$ calculated for all known Laves phase structures of rare earth dialuminides are shown in Table II. The face-centered orthorhombic is the least stable structure, whereas the rhombohedral structure is most favorable. Total energies of the tetragonal and the body centered orthorhombic structures; however, are close to the rhombohedral, indicating possible competition between the ground state structures of $TmAl_2$. The substantial energy difference between the room temperature cubic and three possible ground state structures suggests a potential for discontinuous, i.e. first order change. Further, LSDA+U+SOC with $U = 6.7$ eV and $J = 0.7$ eV within FP-LAPW method with magnetic moments aligned along the [001], [110], and [111] directions in the lowest energy rhombohedral structure indicate [111] as the easy magnetization axis, which agrees with the experimental data obtained on the $TmAl_2$ single crystal [4]. Both the magnetic anisotropy and the moments are weakly dependent on the choice of U (the largest difference is between $U = 3.7$ and 5.7 eV), however, the trends remain identical regardless of the value of the on-site 4f electron correlation parameter (Table III). Same calculations for the ground state tetragonal structure of $DyAl_2$ [30] lead to the orbital magnetic moment reduced by more than $3 \mu_B$ when the easy magnetization direction is switched from [111] to [001]. This result is in agreement with a nearly $4 \mu_B$ step observed in the magnetization of $DyAl_2$ upon application of the magnetic field along the [111] direction (see Fig. 4.18 in Ref.

4]. Unlike TmAl_2 , the calculated magnetic anisotropy and moments of DyAl_2 are nearly independent of the value of the onsite $4f$ electron correlation parameter (U) (see Table III).

Both the occupied and unoccupied $4f$ densities of states (DOS) split, and their degeneracies are partially, yet differently lifted due to CEF and distorted tetrahedral site symmetry in the rhombohedral TmAl_2 (Fig. 10c) and tetragonal DyAl_2 (Fig. 10a). This gives rise to different shapes of effective $4f$ charge densities (and thus the derived energy densities as explained below) in the ground states of these parent binaries. Further, the $4f$ orbital moment in TmAl_2 is quenched and, therefore, the total theoretically derived moment of $6.82 \mu_B/\text{Tm}$ is lower than the expected Hund's rule moment of $7 \mu_B/\text{Tm}$, but it remains somewhat higher than the saturated magnetization of $6.41 \mu_B/\text{Tm}$ derived experimentally. On the other hand, the orbital moment of Dy $4f$ ($4.96 \mu_B/\text{Dy}$) in DyAl_2 is quenched only nominally. Because of the spin polarized $5d$ moments in DyAl_2 , which are non-negligible but small in the TmAl_2 , the calculated total moment ($10.11 \mu_B/\text{Dy}$) is slightly higher than both the Hund's rule moment ($10 \mu_B/\text{Dy}$) and experimental value of $9.95 \mu_B$. When both Tm and Dy atoms are present in pseudo-binaries, the split $4f$ states are added in both spin-up and spin-down channels, as shown for $\text{Tm}_{0.75}\text{Dy}_{0.25}\text{Al}_2$ in Fig. 10b, and the calculated average magnetic moment follows the de Gennes rule and agrees with the experimental results. The effective shape of charge density also changes in comparison with the pure DyAl_2 and TmAl_2 .

Because both spin up and spin down $5d$ states near the Fermi level are provided by Dy, in Tm-rich alloys their role is diminished, and the physical behaviors are expected to resemble those of pure TmAl_2 . Similar to the $4f$ states and because of the tetrahedral and octahedral site

symmetries of R and Al atoms, respectively, $5d$ states are crystal field-split across the Fermi level in RAI_2 . Only a minor $5d$ exchange splitting without a clear DOS peak is found at the Fermi level of the rhombohedral $TmAl_2$ (Fig. 10c'), signaling a weak ferromagnetic state as the local $4f$ moments are aligned ferromagnetically. The rhombohedral distortion in $TmAl_2$ involves crystallographic splitting of the Al site possibly lowering the formation energy at 0 K for the rhombohedral $TmAl_2$ when compared to the tetragonal $DyAl_2$ where all Al atoms remain symmetrically equivalent. However, the total energies of both the tetragonal (for the high concentration of Dy) and rhombohedral (for the high concentration of Tm) structures increase for $x = 0.875$ and 0.5 in $Tm_xDy_{1-x}Al_2$ and, indeed, no structural distortion was observed experimentally for $x = 0.5$ down to 5 K (Fig. 2). Unfortunately, the two high-Tm compositions that appear most interesting, exhibit additional transitions below 5 K, which is out of reach for our low temperature x-ray powder diffraction setup.

The anisotropic energy density relation (energy density expansion within the framework of spherical harmonics) $\frac{E_a}{V} \approx \frac{\kappa_2}{2}(3\cos^2\theta - 1) + \frac{\kappa_4}{8}(35\cos^4\theta - 30\cos^2\theta + 3)$ [31, 32, 33] provides anisotropic energy landscapes, where κ_2 (second order) and κ_4 (fourth order) coefficients are products of the corresponding quadrupolar/octopolar moments and crystal field parameters within the crystal environment. Assuming Tm_xDy_{1-x} a pseudo-atom with molar-average $4f$ electron count between $4f^9$ (Dy) and $4f^{12}$ (Tm) in $Tm_xDy_{1-x}Al_2$ the anisotropic energy landscapes calculated by including only κ_2 are different for different x : they are prolate for $x = 1$ and 0.875 , nearly spherical for $x = 0.5$, and oblate for $x = 0$ (Fig. 11a,b,c,d). As suggested in Ref. 31, the anisotropic shapes may indicate uniaxial anisotropy supporting tetragonal ([001] direction), orthorhombic ([110] direction), and rhombohedral ([111] direction) distortions of the

cubic C15 Laves phase structures. The tetragonal and rhombohedral distortions are indeed supported in DyAl_2 by experimental observation [30] and TmAl_2 by total energy calculation, respectively. It is, therefore, apparent that the anisotropic energy densities may be linked to the crystal distortions. On the contrary, the nearly spherical energy density when $x = 0.5$ indicates vanishing magnetic anisotropy that requires no structural distortion. Previously reported theoretical results suggest that given the crystal field splitting in the pseudo-binary system $\text{Tm}_x\text{Dy}_{1-x}\text{Al}_2$ around the specific concentration $x = 0.5$ the quadrupolar moment changes the sign leading to the sign change in the anisotropy constant [15]. On the other hand, the anisotropic energy landscapes calculated by including both quadrupolar and octopolar coefficients for TmAl_2 and $\text{Tm}_{0.875}\text{Dy}_{0.125}\text{Al}_2$ show dumbbell like shapes which are completely different (Fig. 11a' and b') from those calculated employing only quadrupolar moments. These shapes are quite close to the elemental Er and Sm, where room-temperature hexagonal structures distort trigonally upon cooling [31]. This is in agreement with the rhombohedral distortion found from total energy analysis (see above). The dumbbells shrink along their axis for $\text{Tm}_{0.5}\text{Dy}_{0.5}\text{Al}_2$ (Fig. 11c') suggesting diminished rhombohedral distortion. However, calculations show easy cone $4f$ anisotropy for DyAl_2 (Fig. 11d') that may lead to canted magnetism as suggested from the magnetization direction dependent total energy calculations and earlier single crystal experiment [4].

Conclusions

Experimental and theoretical study of crystal structure, magnetization, heat capacity, and ac magnetic susceptibility of $\text{Tm}_x\text{Dy}_{1-x}\text{Al}_2$ compounds indicate a complex evolution of both magnetic

and lattice ground state structures with x . Heat capacity and magnetization measurements show two distinct regions below T_C : for $x \leq 0.75$ the alloys show typical second-order behavior at ferromagnetic ordering transition, and for $x > 0.85$ one or more additional anomalies present below T_C in both heat capacity and magnetization data, suggesting first-order phase transitions. Temperature dependent powder X-ray diffraction for $x = 0.5$ clearly shows anomaly in the lattice parameter at T_C , however no structural distortion is observed down to 5 K for $x = 0.5$. Calculations indicate that the anisotropic energy densities may be linked to the crystal distortions, however, the nearly spherical energy density when $x = 0.5$ indicates vanishing magnetic anisotropy that requires no structural distortion. The magnetization direction dependent calculations using the tetragonal structure of $DyAl_2$ confirm the substantial orbital magnetic moment reduction when magnetic moments are aligned in the [111] direction as compared to the [001] direction. Same calculations indicate [111] direction as the easy magnetization direction in ferromagnetic rhombohedral $TmAl_2$.

Acknowledgements

The Ames Laboratory is operated for the U. S. Department of Energy (DOE) by Iowa State University of Science and Technology under contract No. DE-AC02-07CH11358. This work was supported by the Office of Science of the U.S. DOE, Division of Materials Sciences and Engineering, Office of Basic Energy Sciences.

TABLE I. Lattice constants and magnetic parameters obtained for $\text{Tm}_x\text{Dy}_{1-x}\text{Al}_2$ compounds.* Curie temperature T_c is obtained from $M(T)$ curves measured at 100 Oe.

Compound	a (Å)	T_c^* (K)	Θ_P^{**} (K)	M_{sat}^{***} ($\mu_B/\text{f.u.}$)	M_{sat} (calc.) ($\mu_B/\text{f.u.}$)	p_{eff}^{**} ($\mu_B/\text{f.u.}$)	p_{eff} (calc.) ($\mu_B/\text{f.u.}$)
TmAl_2	7.7735(1)	3.8	3.4	6.41	7	6.76	7.57
$\text{Tm}_{0.95}\text{Dy}_{0.05}\text{Al}_2$	7.7786(1)	5.9	5.8	-	7.15	7.16	7.72
$\text{Tm}_{0.9}\text{Dy}_{0.1}\text{Al}_2$	7.7823(1)	8.5	8.5	-	7.3	7.17	7.88
$\text{Tm}_{0.85}\text{Dy}_{0.15}\text{Al}_2$	7.7857(1)	10.9	11.2	-	7.45	7.72	8.03
$\text{Tm}_{0.75}\text{Dy}_{0.25}\text{Al}_2$	7.7944(1)	15.8	15.8	7.55	7.75	8.08	8.34
$\text{Tm}_{0.5}\text{Dy}_{0.5}\text{Al}_2$	7.8105(2)	31.2	30.1	8.17	8.5	9.09	9.10
$\text{Tm}_{0.25}\text{Dy}_{0.75}\text{Al}_2$	7.8265(1)	47.9	49.6	9.24	9.25	9.82	9.87
DyAl_2	7.8424(1)	62.1	62.5	9.95	10	10.6	10.63

** Paramagnetic Curie temperature Θ_P and effective paramagnetic moment p_{eff} are obtained

from ac susceptibility measurements.

*** Saturation magnetization is extrapolated from $M(H)$ curves at 2 K. The errors in magnetization values are ~1% or smaller [19]

Table II. Total energies of TmAl_2 for possible Laves phase structures such as cubic ($Fd\bar{3}m$), tetragonal ($I4_1/amd$), body centered orthorhombic ($Imma$), face centered orthorhombic ($Fddd$), and rhombohedral ($R\bar{3}m$).

Structure	Total energy (meV/f.u.) relative to the least stable structure taken at 0 K
Cubic ($Fd\bar{3}m$)	-0.74
Tetragonal ($I4_1/amd$)	-413.31
Body centered orthorhombic ($Imma$)	-413.72
Face centered orthorhombic ($Fddd$)	0
Rhombohedral ($R\bar{3}m$)	-414.95

Table III. On-site $4f$ electron correlation parameter (U) dependent orbital magnetic moments with the moments along the [111] and the [001] directions of the tetragonal DyAl_2 and rhombohedral TmAl_2 .

System	Orbital magnetic moment in μ_B		
	$U = 3.7 \text{ eV}$	$U = 5.7 \text{ eV}$	$U = 6.7 \text{ eV}$
DyAl_2 [001]	4.95	4.93	4.94
DyAl_2 [111]	1.79	1.74	1.72
TmAl_2 [001]	2.10	2.53	2.67
TmAl_2 [111]	2.41	2.65	2.72

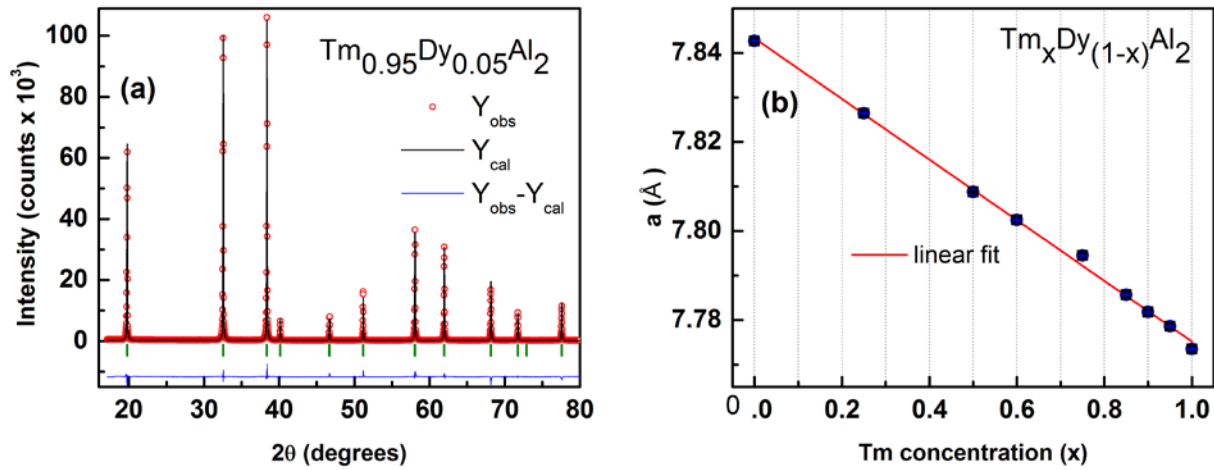


FIG. 1. (Color online) (a) Rietveld refinement of the room temperature XRD pattern (Cu $K\alpha_1$ radiation) for $\text{Tm}_{0.95}\text{Dy}_{0.05}\text{Al}_2$. (b) Room temperature lattice parameter a as a function of Tm concentration for $\text{Tm}_x\text{Dy}_{1-x}\text{Al}_2$ (right). Error bars in Fig. 1b are smaller than the sizes of the symbols.

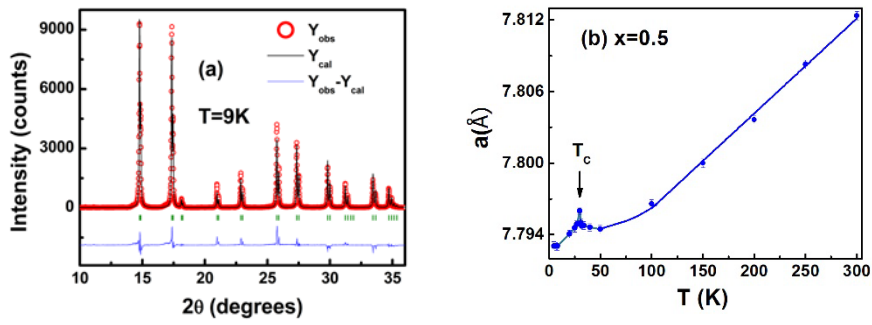


FIG. 2. (Color online) (a) Rietveld refinement of the XRD pattern (Mo $K\alpha$ radiation) for $\text{Tm}_{0.5}\text{Dy}_{0.5}\text{Al}_2$ at $T = 9\text{ K}$. (b) Lattice parameter a as a function of temperature (obtained from Rietveld refinement of XRD data) for $\text{Tm}_{0.5}\text{Dy}_{0.5}\text{Al}_2$.

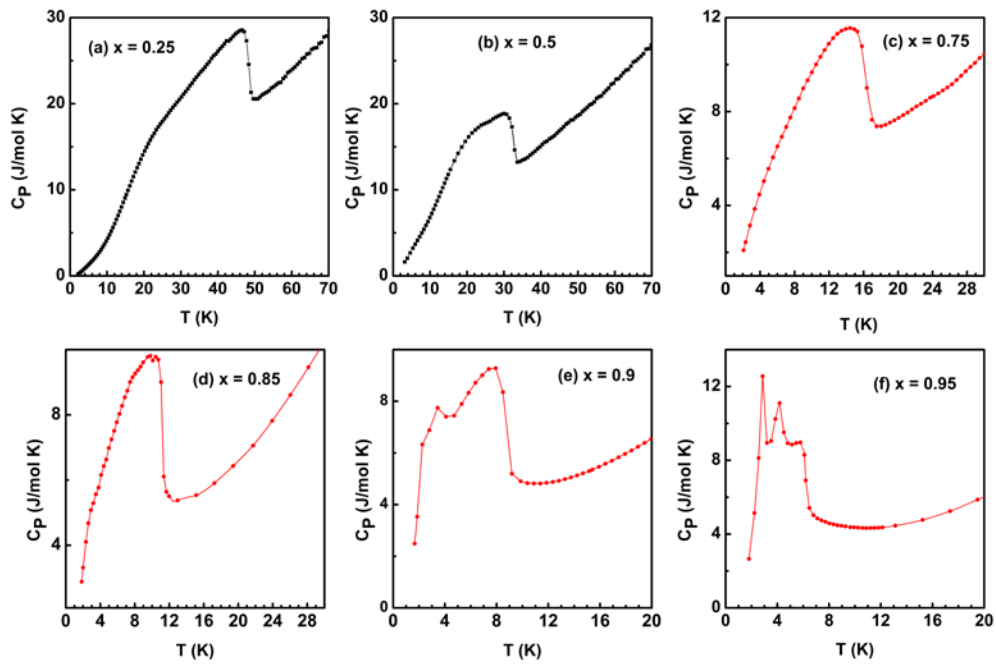


FIG. 3. (Color online) (a-f) Heat capacity as a function of temperature measured at zero field for $Tm_xDy_{1-x}Al_2$ with $x = 0.25, 0.5, 0.75, 0.85, 0.9,$ and 0.95 .

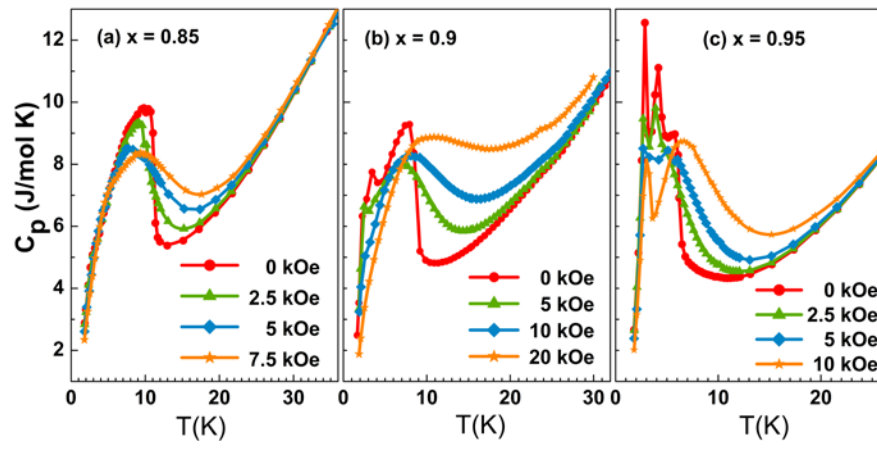


FIG. 4. (Color online) Heat capacity vs temperature for $Tm_xDy_{1-x}Al_2$ (a) $x = 0.85$, (b) $x = 0.9$, and (c) $x = 0.95$ measured at different applied magnetic fields.

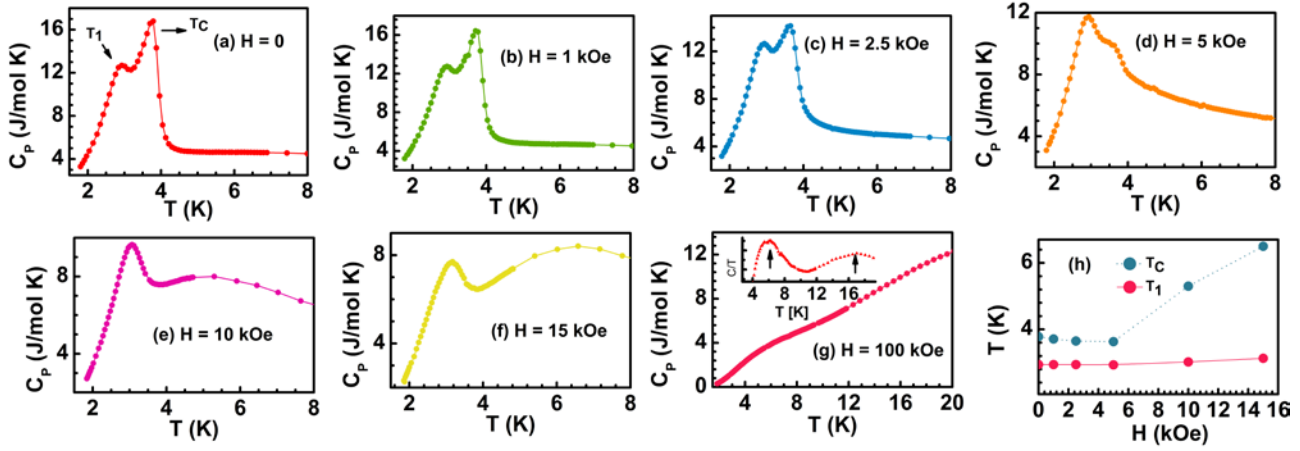


FIG. 5. (Color online) (a-g) Heat capacity vs temperature measured at magnetic fields up to 100 kOe for $TmAl_2$. (h) Field dependence of the Curie temperature T_C and the temperature of the anomaly (T_1). Inset in (g) shows C/T vs. T for the data presented in (g).

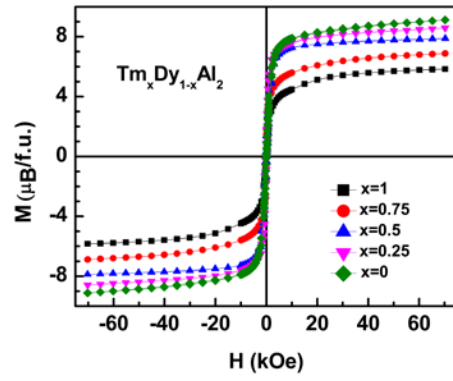


FIG. 6. (Color online) Magnetization as a function of applied magnetic field measured at 2 K under dc fields up to 70 kOe for $Tm_xDy_{1-x}Al_2$ with $x = 0, 0.25, 0.5, 0.75,$ and 1.

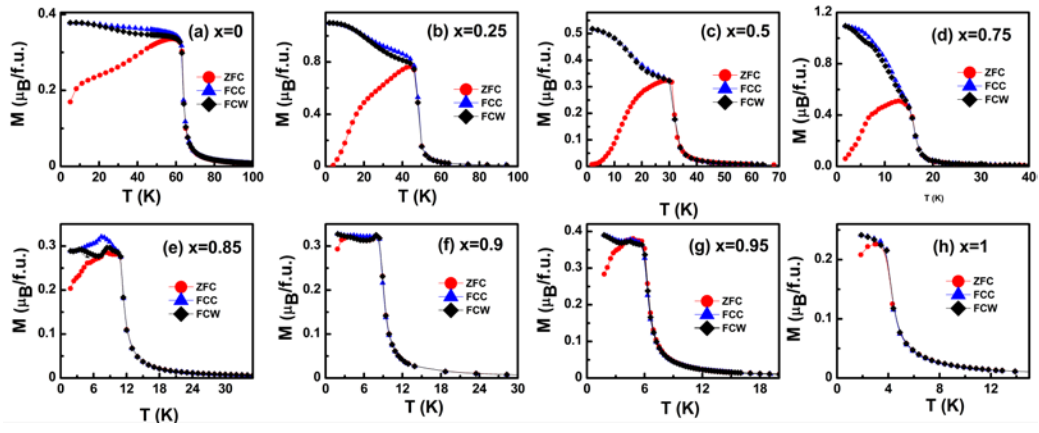


FIG. 7. (Color online) Magnetization as a function of temperature measured at $H = 0.1$ kOe for $\text{Tm}_x\text{Dy}_{1-x}\text{Al}_2$ with $x = 0, 0.25, 0.5, 0.75, 0.85, 0.9, 0.95,$ and 1 .

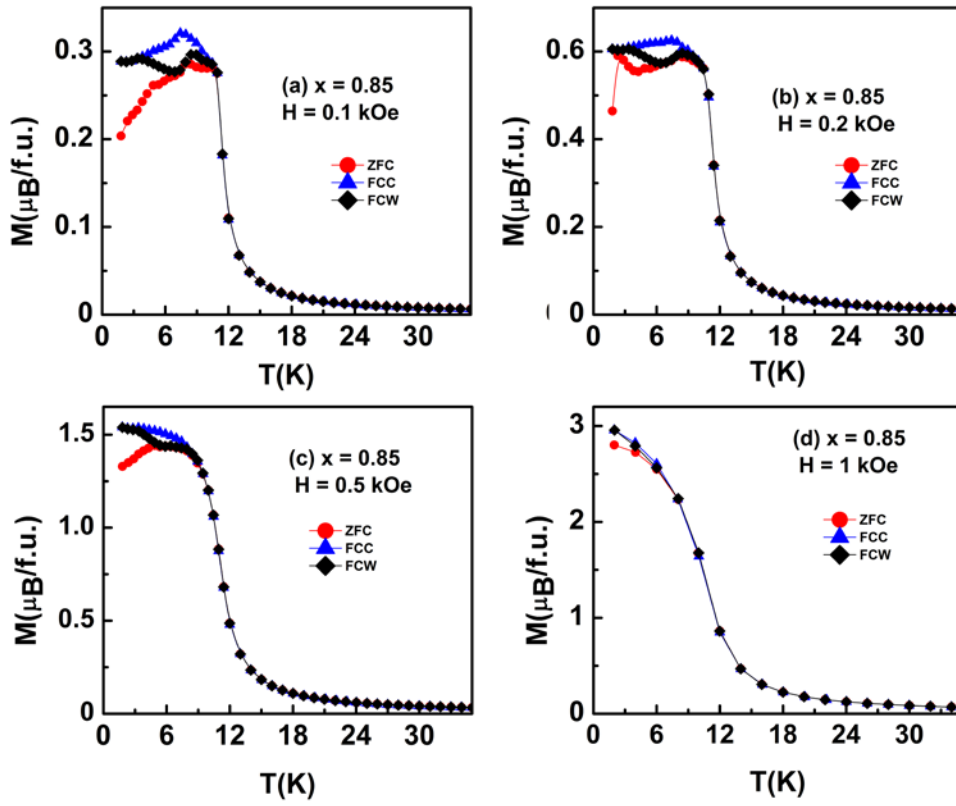


FIG. 8. (Color online) Magnetization as a function of temperature measured at different magnetic fields for $\text{Tm}_{0.85}\text{Dy}_{0.15}\text{Al}_2$.

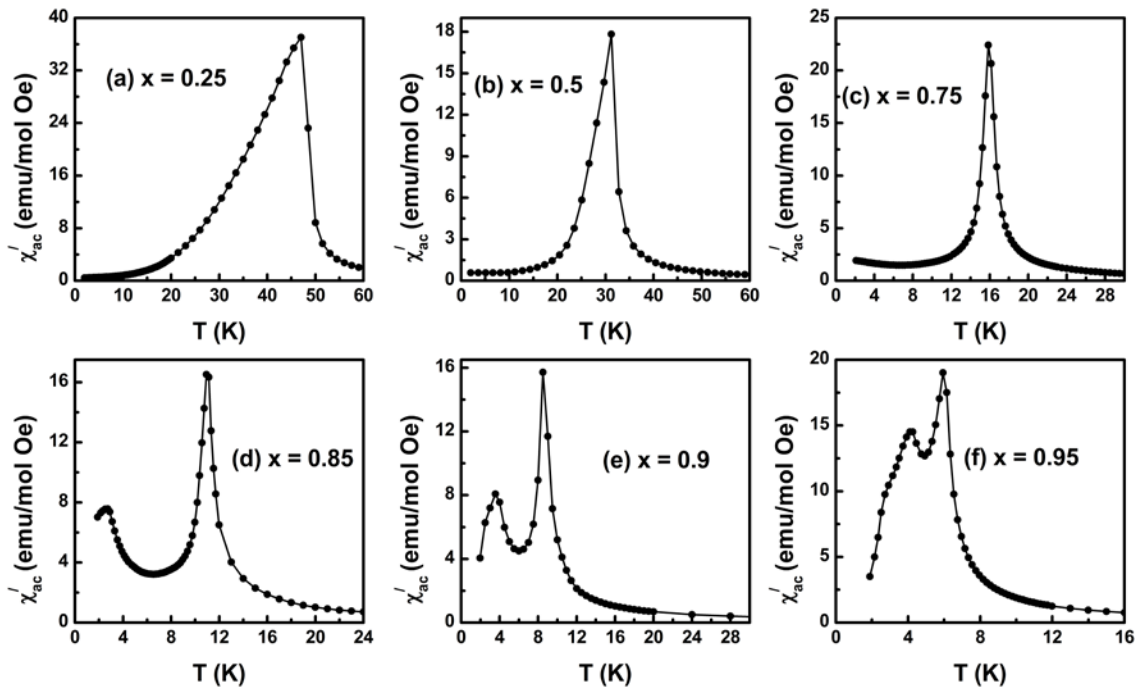


FIG. 9. (Color online) Real part of ac magnetic-susceptibility vs. temperature measured for $\text{Tm}_x\text{Dy}_{1-x}\text{Al}_2$ with $x = 0.25, 0.5, 0.75, 0.85, 0.9,$ and 0.95 .

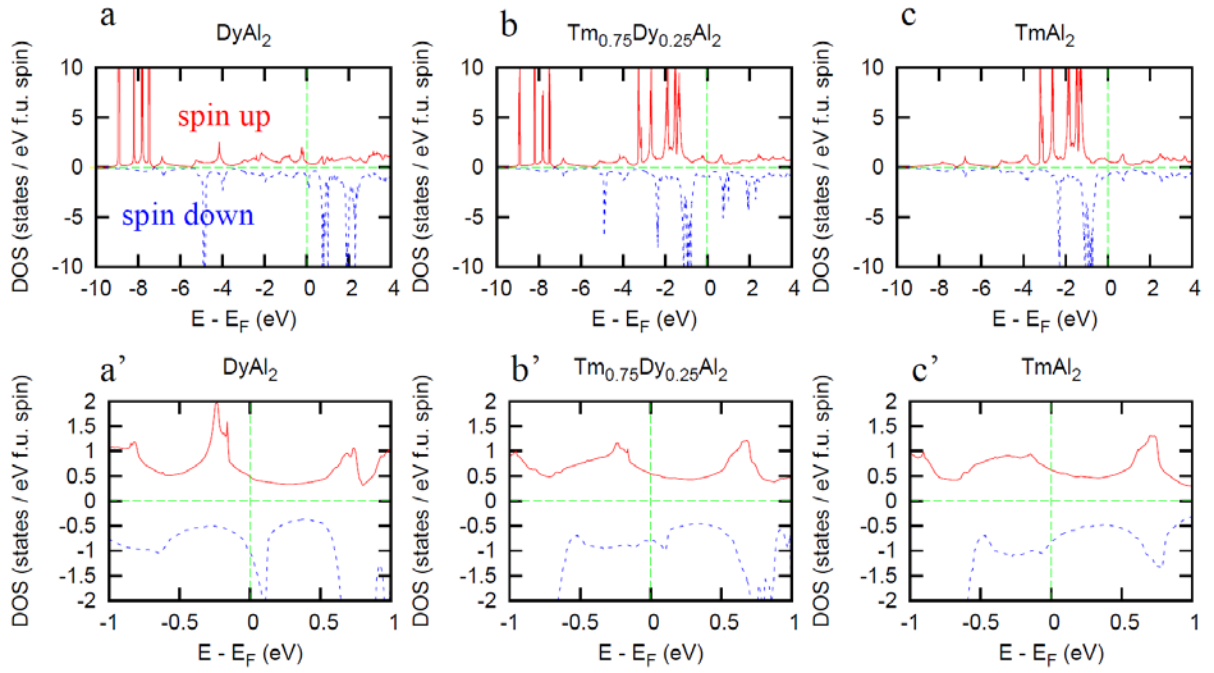


FIG. 10. The total density of states (DOS) of the ground state (a) tetragonal DyAl_2 , (b) cubic $\text{Tm}_{0.75}\text{Dy}_{0.25}\text{Al}_2$, and (c) rhombohedral TmAl_2 . (a', b', c') represent the DOS close to the Fermi level for clarity.

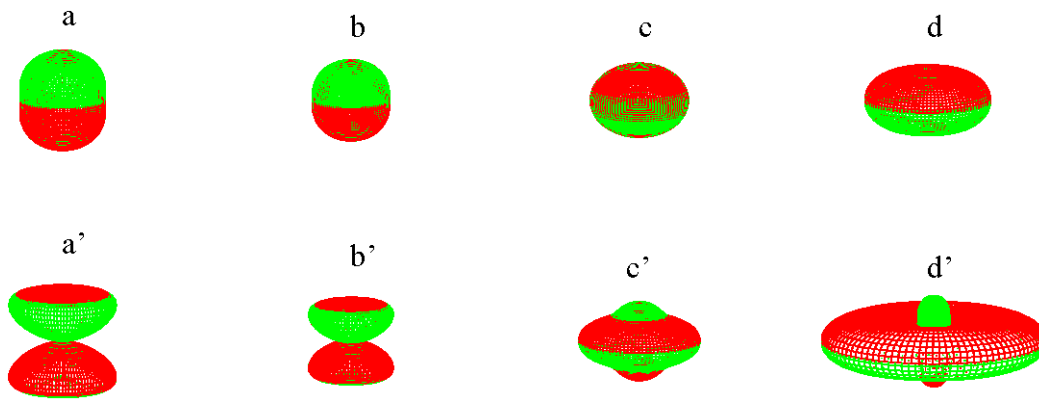


FIG. 11. Anisotropic $4f$ energy density including the contributions from quadrupolar only (a, b, c, d) and quadrupolar and octopolar (a' , b' , c' , d') moments of $Tm_xDy_{1-x}Al_2$ ($x = 1.0, 0.875, 0.5,$ and 0). The magnitudes of octopolar moments $Q_4/\langle r^4 \rangle_{4f}$ are slightly higher than those of the corresponding quadrupolar moments $Q_2/\langle r^2 \rangle_{4f}$.

References

-
- ¹ F. R. Arantes, D. Aristizábal-Giraldo, S. H. Masunaga, F. N. Costa, F. F. Ferreira, T. Takabatake, L. Mendonça-Ferreira, R. A. Ribeiro, and M. A. Avila, Structure, magnetism, and transport of single-crystalline RNiSi₃(R = Y, Gd-Tm, Lu), *Phys. Rev. Mat.* 2 (2018) 044402.
- ² L. V. B. Diop and O. Isnard, Multiple magnetization steps and plateaus across the antiferromagnetic to ferromagnetic transition in La_{1-x}Ce_xFe₁₂B₆: Time delay of the metamagnetic transitions, *Phys. Rev. B* 97 (2018) 014436.
- ³ Dm. M. Korotin, S. V. Streltsov, E. G. Gerasimov, N. V. Mushnikov, I. S. Zhidkov, A. I. Kukharenko, L. D. Finkelstein, S. O. Cholakh, and E. Z. Kurmaev, Magnetic ordering in intermetallic La_{1-x}Tb_xMn₂Si₂, *J. Magn. Magn. Mat.* 454 (2018) 144.
- ⁴ H. G. Purwins, and A. Leson, Magnetic properties of (rare earth)Al₂ intermetallic compounds, *Adv. in Phys.* 39 (1990) 309.
- ⁵ H. G. Purwins, E. Walker, B. Barbara, M. F. Rossignol, P. Bak, Magnetization, magnetocrystalline anisotropy and the crystalline electric field in (rare earth) Al₂ compounds *J. Phys: C: Solid State. Phys.* 7 (1974) 3573.
- ⁶ A. L. Lima, K. A. Gschneidner, Jr, V. K. Pecharsky, A. O. Pecharsky, Disappearance and reappearance of magnetic ordering upon lanthanide substitution in (Er_{1-x}Dy_x)Al₂, *Phys. Rev. B* 68 (2003) 134409.
- ⁷ R. Nirmla, Y. Mudryk, V. K. Pecharsky, K. A. Gschneidner, Jr., Unusual magnetism of Er_{0.75}Dy_{0.25}Al₂ *Phys. Rev. B* 76 (2007) 014407.

-
- ⁸ Y. G. Xiao, Q. Huang, Z. W. Ouyang, F. W. Wang, J. W. Lynn, J. K. Liang, and G. H. Rao, Canted magnetic structure arising from rare-earth mixing in the Laves-phase compound $(\text{Nd}_{0.5}\text{Tb}_{0.5})\text{Co}_2$, *Phys. Rev. B* 73 (2006) 064413.
- ⁹ A. Murtaza, S. Yang, T. Chang, A. Ghani, M. T. Khan, R. Zhang, C. Zhou, X.g Song, M. Suchomel, and Y. Ren, *Phys. Rev. B* **97**, 104410 (2018).
- ¹⁰ A. L. Lima, A. O. Tsokol, K. A. Gschneidner, Jr., V. K. Pecharsky, T. A. Lograsso, D. L. Schlagel, Magnetic properties of single-crystal DyAl_2 , *Phys. Rev. B* 72 (2005) 024403.
- ¹¹ H. Adachi, H. Ino, A ferromagnet having no net magnetic moment, *Nature (London)* 401 (1999) 148.

-
- ¹² P. D. Kulkarni, A. Thamizhavel, V. C. Rakhecha, A. K. Nigam, P. L. Paulose, S Ramakrishnan, A. K. Grover, Magnetic compensation phenomenon and the sign reversal in the exchange bias field in a single crystal of Nd_{0.75}Ho_{0.25}Al₂, European Phys. Lett. 86 (2009) 47003.
- ¹³ A. K. Pathak, D. Paudyal, W. T. Jayasekara, S. Calder, A. Kreyssig, A. I. Goldman, K. A. Gschneidner, Jr., V. K. Pecharsky, Unexpected magnetism, Griffiths phase, and exchange bias in the mixed lanthanide Pr_{0.6}Er_{0.4}Al₂, Phys. Rev. B 89 (2014) 224411.
- ¹⁴ A. F. Deutz, H. B. Brom, W.J. Huiskamp, L. J. de Jongh, Low temperature specific heat and a.c. susceptibility of TmAl₂, Solid State Commun. 68 (1988) 803.
- ¹⁵ D. Paudyal, A. K. Pathak, V. K. Pecharsky, K. A. Gschneidner, Understanding and prediction of electronic-structure-driven physical behaviors in rare-earth compounds, Jr., J. Phys.: Condens. Matter 25 (2013) 396002.
- ¹⁶ A. P. Holm, V. K. Pecharsky, K. A. Gschneidner, Jr, X-ray powder diffractometer for *in situ* structural studies in magnetic fields from 0 to 35 kOe between 2.2 and 315 K, Rev. Sci. Instrum 75 (2004) 1081.
- ¹⁷ B. Hunter, Rietica-A Visual Rietveld Program, International Union of Crystallography Commission on Powder Diffraction Newsletter No. 20, (Summer 1998) [<http://www.rietica.org>].
- ¹⁸ V. K. Pecharsky, J. O. Moorman, and K. A. Gschneidner, Jr., Rev. Sci. Instrum. **68**, 4196 (1997).
- ¹⁹ V.I. Zverev, R.R.Gimaev, A. M. Tishin, Ya. Mudryk, K. A.GschneidnerJr., V. K. Pecharsky, The role of demagnetization factor in determining the ‘true’ value of the Curie temperature, J. Magn. Magn. Mat 323 (2011) 2453.

-
- ²⁰ V. I. Anisimov, F. Aryasetiawan, A. I. Lichtenstein, First-principles calculations of the electronic structure and spectra of strongly correlated systems: the LDA+ U method, *J. Phys.: Condens. Matter.* 9 (1997) 767.
- ²¹ O. K. Andersen, and O. Jepsen, Explicit, first-principles tight-binding theory *Phys. Rev. Lett.* 53 (1984) 2571.
- ²² P. Blaha, K. Schwarz, G. Madsen, D. Kvasnicka, J. Luitz, 2001 *WIEN2k*, An Augmented Plane Wave + Local Orbitals Program for Calculating Crystal Properties (Karlheinz Schwarz, Techn. Universität Wien, Austria), ISBN 3-9501031-1-2.
- ²³ I. R. Harris, R. C. Mansey, G. V. Raynor, Rare earth intermediate phases: III. The cubic laves phases formed with aluminium and cobalt, *J. Less-Common Metals* 9 (1965) 270.
- ²⁴ T. Inoue, S. G. Sankar, R. S. Craig, W. E. Wallace and K. A. Gschneidner, Jr., Low temperature heat capacities and thermal properties of DyAl₂, ErAl₂ and LuAl₂, *J. Phys. and Chem. Solids* 38 (1977) 487.
- ²⁵ W. Schelpm, W. Drewes, A. Leson, H.-G. Purwins, Low temperature heat capacity of some heavy REAl₂ compounds (RE = Tb, Dy, Er and Tm) in a magnetic field, *J. Phys. and Chem. of Solids* 47, (1986) 855 .

-
- ²⁶ D. Kohake, A. Leson, H. G. Purwins, A. Furrer, Magnetization behaviour of DyAl₂ single crystals Solid State Commun. 43, (1982) 965.
- ²⁷ S. Horn, M. Loewenhaupt, H. Scheuer, F. Steglich, Magnetic order and crystal fields in TmAl₂ and disordered (Tm, La) Al₂ alloys, J. Magn. Magn. Mat. 14 (1979) 239.
- ²⁸ S. Jia, N. Ni, S. L. Bud'ko, and P. C. Canfield, Magnetic properties of RFe₂Zn₂₀ and RCo₂Zn₂₀ (R=Y, Nd, Sm, Gd–Lu), Phys. Rev. B 80 (2009) 104403.
- ²⁹ V. V. Novikov, E.S.Pilipenko, S. L. Bud'ko, Crystal electric field effects and thermal expansion of rare-earth hexaborides, Solid State Communication 252 (2017) 51.
- ³⁰ M. Khan, A. K. Pathak, Y. Mudryk, K. A. Gschneidner, Jr., V. K. Pecharsky, Anisotropy induced anomalies in Dy_{1-x}Tb_xAl₂, J. Mat. Chem. C 5 (2017) 896.
- ³¹ R. Skomski, Simple Models of Magnetism (Oxford: Oxford University Press), chapter 3, p 93 and references therein (2006).
- ³² A. J. Freeman, R. E. Watson, Theoretical investigation of some magnetic and spectroscopic properties of rare-earth ions, Phys. Rev. 127 (1962) 2058.
- ³³ P. Fulde, Crystal Fields in *Hand Book on the Physics and Chemistry of Rare Earths*. eds Gschneidner, Jr, KA, Eyring L (North-Holland, Amsterdam, New York, Oxford), Vol. 2, p. 295 (1979).